JOURNAL OF SYNCHROTRON RADIATION

ISSN 1600-5775

Received 24 July 2014
Accepted 6 March 2015

Edited by D. A. Reis, SLAC National Accelerator Laboratory, USA

Keywords: nanocalorimetry; thin-film stack; WAXS.

Simultaneous nanocalorimetry and fast XRD measurements to study the silicide formation in Pd/a-Si bilayers

Manel Molina-Ruiz,[a] Pablo Ferrando-Villalba,[a] Cristian Rodríguez-Tinoco,[a] Gemma Garcia,[a] Javier Rodríguez-Viejo,[a] Inma Peral[b] and Aitor F. Lopeandía[a]*

[a]Departament de Física, Universitat Autònoma de Barcelona, Cerdanyola del Vallès, 08193, Spain, and [b]ALBA Synchrotron Radiation Facility, Cerdanyola del Vallès 08290, Spain.
*Correspondence e-mail: aitor.lopeandia@uab.cat

The use of a membrane-based chip nanocalorimeter in a powder diffraction beamline is described. Simultaneous wide-angle X-ray scattering and scanning nanocalorimetric measurements are performed on a thin-film stack of palladium/amorphous silicon (Pd/a-Si) at heating rates from 0.1 to 10 K s^{-1}. The nanocalorimeter works under a power-compensation scheme previously developed by the authors. Kinetic and structural information of the consumed and created phases can be obtained from the combined techniques. The formation of Pd_2Si produces a broad calorimetric peak that contains overlapping individual processes. It is shown that Pd consumption precedes the formation of the crystalline Pd_2Si phase and that the crystallite size depends on the heating rate of the experiment.

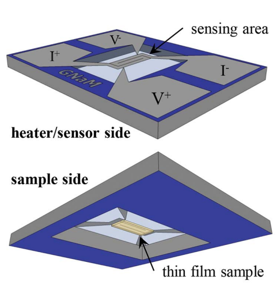

1. Introduction

Calorimetry is a well known technique that is used to explore the kinetics and thermodynamics of phase formation between pairs of materials when they are submitted to thermal treatments (Ma *et al.*, 1991; Michaelsen *et al.*, 1997). If the solids are in thin-film form the amount of material is typically too small to be directly measured by conventional differential scanning calorimetry. A useful strategy such as using multilayers consisting of many repetitions of the fundamental A/B stack is often used to increase the analysed mass and resolve the calorimetric transitions (Spaepen & Thompson, 1989). However, this approach does not realistically reproduce the systems at use in real applications, which often involve single layers or bilayer (Orava *et al.*, 2012). Needless to say, calorimetry lacks the structural information required to correlate the observed thermodynamic phase transitions to structural changes in the sample. Simultaneous X-ray scattering and calorimetry experiments using standard-type calorimeters have been successfully attempted in the past (Lexa, 1999; Nemouchi *et al.*, 2005). However, standard calorimeters are often not well suited for complementary X-ray diffraction (XRD) analysis. The field of simultaneous synchrotron and complementary techniques to characterize phase formation is gaining attention in the scientific community as a way to fully characterize the system under study (Gregoire *et al.*, 2012; Marcelli *et al.*, 2012; Zalden *et al.*, 2012; Xiao *et al.*, 2013; Rosenthal *et al.*, 2014). The new generation of wide-angle and fast detectors is also helping to monitor phase changes at faster rates and with unprecedented spatial and temporal resolution, opening a vast field of exploration in materials science. In this respect, membrane-based calorimeters provide a unique platform to combine the easy thin-film geometry for X-ray characterization with the high sensitivity of the nanocalorimeter to resolve phase transitions in samples of mass as small as a few nanograms (Zhang *et al.*, 2002; Molina-Ruiz *et al.*, 2011). Of interest to the silicide phase formation analysed here, previous works in recent years have addressed the use of synchrotron X-ray beams and simultaneous resistive measurements to characterize intermetallic phase formation in Si couples (Smeets *et al.*, 2008; Putero *et al.*, 2013).

In this report, we present the build-up, calibration and testing of a new setup which combines membrane-based nanocalorimetry with XRD measurement at the MSPD beamline of the ALBA synchrotron. The setup is used to follow the kinetics and structure of phase formation during the palladium/amorphous silicon (Pd/a-Si) bilayer reaction during temperature up-scans at various heating rates.

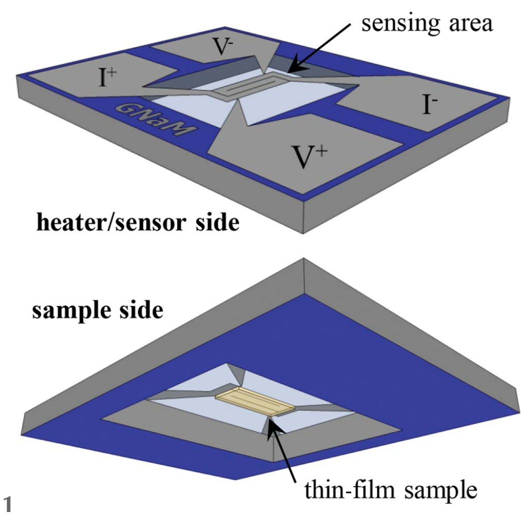

Figure 1
Schematics of a nanocalorimeter projection from the top and bottom sides.

2. Experimental

Simultaneous *in situ* XRD and nanocalorimetry measurements monitoring the solid state phase formation of palladium silicide, Pd_2Si, during the thermal processing of Pd/a-Si bilayers were performed at the MSPD beamline of the ALBA synchrotron (Barcelona, Spain). In this section we describe the experimental developments required for that purpose.

2.1. Nanocalorimeter

The nanocalorimeter consists of a free-standing dielectric membrane of 180/50 nm-thick SiN_x/SiO_2 supported on a massive Si frame. The dielectric membrane is used as a light mechanical substrate to build on top the calorimetric cell. In the centre of the membrane a thin-film bilayer of 10/100 nm Ti/Pt is patterned by lithography defining the metallic element used both as resistive heater and thermometer. The platinum thin film, used as a resistance temperature detector, exhibits a linear dependence of its electrical resistance with temperature. Each device requires a previous calibration which is carried out by measuring its resistance from room temperature up to 500 K into an adapted furnace. Beneath the platinum structure, at the other side of the dielectric membrane, the sample can be evaporated using a microfabricated shadow mask which delimits the deposition area (1.085 mm^2), at the centre of the calorimetric cell. The heater/sensor element is designed to locally release power and measure the temperature in a four-wire configuration. A schematic of the nanocalorimetric device showing the sample position is given in Fig. 1. The reduced heat capacity addenda of the calorimetric cell, below 1 $\mu J\ K^{-1}\ mm^{-1}$, is one of the key factors allowing measurements of reactions in ultrathin films as the calorimetric signal of interest is enhanced in comparison with the background noise (essentially proportional to the addenda). Moreover, in calorimetry, the heat capacity signature is proportional to the dynamic range imposed during the temperature scans. The low mass of the calorimetric cell, its high thermal insulation from the surroundings and, above all, the excellent thermal link between the heater/sensor element and the sample, which are separated by a 180–230 nm-thick dielectric membrane, permits the enhancement of the energy resolution achieved during the calorimetric scan. This type of nanocalorimeter has been frequently used to measure phase transitions (Lopeandía *et al.*, 2008*a*; Leon-Gutierrez *et al.*, 2010) in a wide range of heating rates (Lopeandía *et al.*, 2008*b*; Molina-Ruiz *et al.*, 2014).

2.2. Thin-film growth

Thin films of palladium (Pd) and amorphous silicon (a-Si) were grown by electron beam evaporation at room temperature and a pressure of 10^{-6} mbar with a growth rate of 0.1 nm s^{-1}. The film is a bilayer formed of 75 nm a-Si and 60 nm Pd on top. The silicon-based microfabricated shadow mask is used on every nanocalorimeter to limit the deposited film to the sensing area of the device, aligned with the metal heater/sensor. Upon temperature rise and completion of the reaction, a thin film of Pd_2Si, about 100 nm thick, is formed leaving a silicon excess of approximately 30 nm. The obtained Pd_2Si thin-film samples have a mass below 1 μg, which is sufficient for the sensitivity of both the power-compensated nanocalorimetric technique and the fast-XRD acquisition.

2.3. Vacuum chamber

One essential requirement to perform nanocalorimetry is to work under high-vacuum conditions to minimize all heat transfer from the calorimetric cell. Abiding by these conditions the heat released or absorbed in the calorimetric cell will contribute to its inner energy (increasing or decreasing temperature) or will be conducted through the dielectric membrane to the frame (or radiated in the case of high temperatures). For that reason, it was required that a vacuum chamber specially designed to simultaneously perform the nanocalorimetric measurements and the X-ray diffraction experiments in the MSPD beamline was fabricated. The chamber is equipped with two Kapton view ports of 5 cm

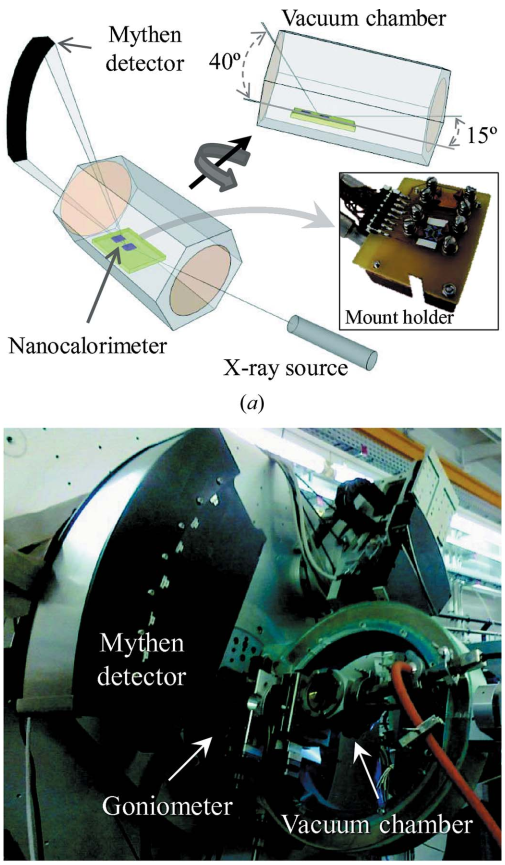

Figure 2
(*a*) Schematic of the experimental setup with the nanocalorimeter inside the vacuum chamber. (*b*) Experimental setup with the vacuum chamber in the centre and Mythen detector on the left.

diameter with a reduced thickness of 25 µm to minimize X-ray absorption. Inside the chamber the calorimeter is loaded into a mount holder that geometrically places the nanocalorimeter at the centre of the goniometer, which is tilted 15° with respect to the incident X-ray beam (Fig. 2*a*). The holder is also used to bring the electrical contacts from the electrical feed-through close to the chip, locally wire-bond the heater/sensor elements and to fix the base temperature using a fluid bath while measuring it with a Pt100 sensor. A schematic view and a labelled photograph of the chamber are shown in Fig. 2.

2.4. XRD and Mythen detector

The beam energy is fixed to 15 keV. The detector is a Mythen type, which is a very fast and sensitive one-dimensional detector, covering an angular range 2θ from 19° to 59°, which allows a high number of counts per unit time to be taken (Knapp *et al.*, 2011). Even so, the very small amount of sample, typically less than 1 µg, imposes a minimum time to acquire a reasonable signal-to-noise signal, around 1 s. As a consequence, the maximum heating rate of the experiments is set to 10 K s^{-1}. With these parameters one X-ray spectrum is recorded every 10 K at the fastest heating rate.

2.5. Nanocalorimetry in power-compensation mode

While the fastest heating rate (10 K s^{-1}) is limited by the Mythen detector owing to the low amount of mass available for X-ray scattering, the lowest heating rate is determined by the sensitivity of the nanocalorimetric technique. It is important to note that, the lower the heating rate is, the lower the resolution of the calorimetric signal. For heating rates in the range from 0.1 to 10 K s^{-1}, the best technique is the so-called power-compensation scanning nanocalorimetry technique and it has already been tested in several systems (Lopeandía *et al.*, 2005, 2008*b*; Molina-Ruiz *et al.*, 2014). Power-compensation scanning nanocalorimetry consists of feeding a device with a DC current whose value is recalculated by means of a proportional and integral (PI) controller to follow a prefixed heating ramp.

The implementation of the PI temperature controller combines a high-resolution sourcemeter (Keithley 2400 source/measure unit), used to generate the current and to measure the voltage drop in the calorimetric cell, and a PC-based program (developed in Labview) with the PI algorithm to govern the source actions *via* GPIB communication protocol. The algorithm includes a feedforward stage in parallel to the feedback loop. A schematic of the power-compensation controller algorithm is shown in Fig. 3. The feedforward stage evaluates *a priori* the gross action based on a simple model of the nanocalorimeter. As the characteristic thermal response of the calorimeter is very fast, we use a steady-state lumped parameter model which considers a calorimetric cell, at a temperature T, linked through the silicon membrane (working in high vacuum), with a thermal conductance K_L, to the silicon frame, at a temperature T_0. By measuring the temperature rise for different input powers with empty devices, K_L can be evaluated as the slope of the plot, obtaining linear behaviours while temperature differences are kept small. In general, K_L is considered as a polynomial function of temperature, which also takes into account radiation losses. In the experiments presented here, the set

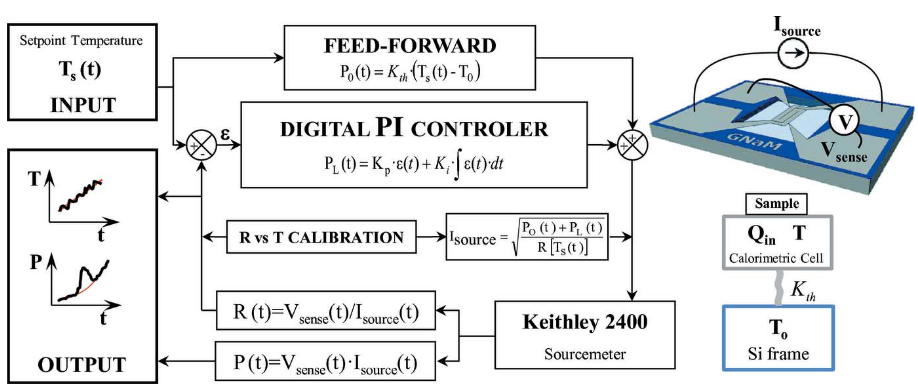

Figure 3
Schematic of the power-compensation controller algorithm.

point temperatures are fixed to evolve linearly defining ramps of constant heating rates. As most of the action is taken in advance by the feedforward stage, the feedback controller only corrects small deviations from the set point values (called error, ε) promoted by the presence of the sample. A selection of the feedback control action proportional to the error $[K_P\varepsilon(t)]$, called the P term (from proportional), added to a term proportional to the accumulated error $[K_I \int \varepsilon(t)\, dt]$, called the I term (from integral), suffices to correct this small deviation.

For calorimetric measurements, the subtraction of the background power result is mandatory. This can be done by either acquiring a reference signature from a previous calibration measurement or, in the case of analysing non-reversible transformations, by using subsequent scans as reference measurements. The GPIB bus communication limits the minimum loop time to 150 ms. For every loop time, we can evaluate the power injected and the temperature of the calorimetric cell from the measurements of current sourced and voltage measured. Working in the better resolution range of the source, we have a noise floor of 25 nW $Hz^{-1/2}$ (peak-to-peak). In steady-state conditions, like those used for the measurements presented here, a careful estimation of power losses is required to obtain accurate heat capacity data. Nevertheless, the formation of the silicide has a great impact on the thermal resistance, and, hence, heat-loss corrections by subtraction of the second scan are not straightforward. In the following, we only provide an apparent value of the heat capacity.

2.6. Alignment procedure

A cumbersome task when both techniques are used simultaneously is beam alignment. In fact, the visible sensing area for the beam is the 15° vertical projection of the real sample area (~1 mm^2), so that the beam dimensions are fixed to 700 µm wide by 300 µm high. The alignment procedure was realised in three steps: (i) Localizing and centring the beam onto the nanocalorimeter with the help of fluorescent paper placed on its edges. (ii) Finding the sensing area using the PI controller as a thermal detector. The use of membrane-based structures allows monitoring the X-ray-induced heating by locally measuring the temperature increase of the sensing area of the device. This temperature rise has been used here to fine-tune the position of the beam with respect to the sample, which is located exactly beneath the Pt heater/sensor. (iii) As the heater is made of Pt, we search for the position that maximizes the Pt X-ray signal in the diffraction pattern. The alignment methodology, which takes full advantage of the membrane-based geometry of the calorimetric chips, allowed a highly time-effective process and was routinely applied to all thin-film samples analysed in this work.

3. Results and discussion

Three Pd (60 nm)/a-Si (75 nm) bilayer samples were measured using nanocalorimetry and X-ray diffraction at three different heating rates: 0.1, 1 and 10 K s^{-1}. The results are shown in Fig. 4. The background of each plot is a two-dimensional map of the X-ray signal as a function of temperature. These two-dimensional maps represent a region about 12° of the total range covered by the Mythen detector. The colour marks the intensity of the signal. The superimposed symbols represent the apparent heat capacity extracted from nanocalorimetry at the three different heating rates. The nanocalorimetric curves are obtained by removing a second scan (baseline) where no reaction takes place. The difference in apparent heat capacity provides information about the kinetics of the silicide formation overcoming the contribution of the addenda. The peak is related to the formation of Pd_2Si during the temperature up-scan and it moves to higher temperatures as the heating rate increases, typical of thermally activated

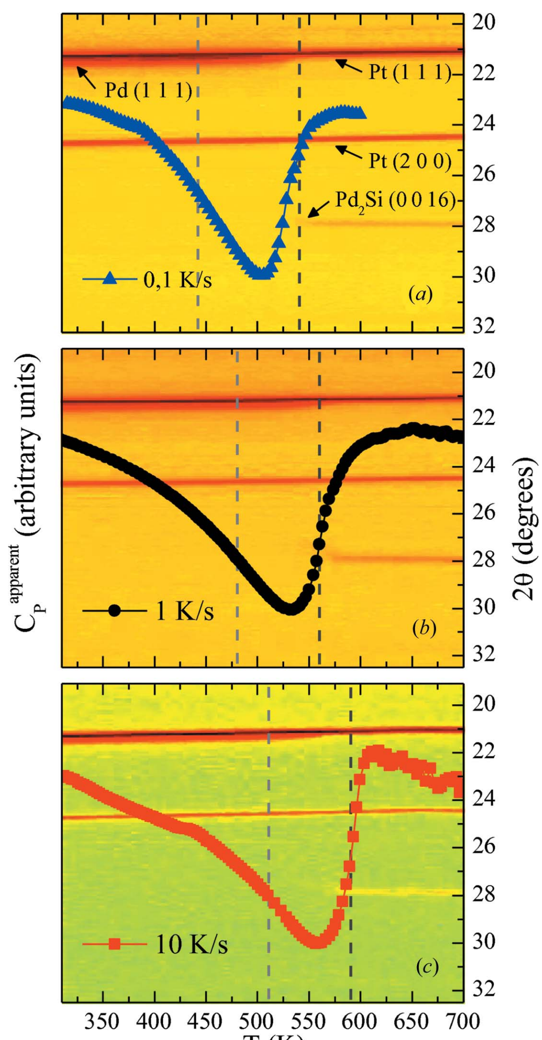

Figure 4
Nanocalorimetric signal (symbols) for samples formed by 75 nm a-Si and 60 nm Pd bilayers at three different heating rates: (*a*) 0.1, (*b*) 1 and (*c*) 10 K s^{-1}. The background of each graph corresponds to a two-dimensional plot of the XRD patterns. Colour variation within each graph indicates the relative intensity of the XRD peaks. Dashed vertical lines mark the onset of Pd consumption (grey) and the appearance of the Pd_2Si diffraction peak (dark grey) obtained from the analysis of the XRD spectra.

processes. The exothermic peaks are wider than those observed in commercial differential scanning calorimetry using samples with much higher mass (Molina-Ruiz *et al.*, 2014). In fact, the broad signals of the various calorimetric traces shown in Fig. 4 include several exothermic peaks that are partially overlapped in temperature. As demonstrated previously (Molina-Ruiz *et al.*, 2014), the main processes involved in the silicide formation are: interdiffusion between Pd and a-Si to form a disordered Pd_xSi_{1-x} phase at the interface, nucleation of Pd_2Si in this mixed region, crystallization of amorphous silicon and vertical growth of Pd_2Si. In this case, owing to the highly energetic reactions, self-heating is considerable and the control of the PI over the heating rate is not fast enough to individually differentiate the partially overlapped processes. Thus a single broad calorimetric peak is measured. The X-ray data of Fig. 4 permit several steps of the solid-state reaction to be followed. The loss of intensity of the Pd peak occurs at much lower temperatures than the onset of the apparent formation of Pd_2Si. Both events are marked as vertical dashed lines in Fig. 4. First, the disappearance of Pd at a temperature that depends on the heating rate (first vertical dashed line of Fig. 4) highlights the partial consumption of Pd to form a noncrystalline Pd_xSi_{1-x} alloy at the interface, indistinguishable in the X-ray spectra. The onset temperatures of Pd consumptions are 440, 480 and 510 K for the 0.1, 1 and 10 K s^{-1} data, respectively. The disappearance of the Pd (111) peak occurs over a temperature interval of 80–100 K and free Pd is completely consumed after the appearance of the Pd_2Si (0 0 16) diffraction peak. At temperatures of 540 K (0.1 K s^{-1}), 560 K (1 K s^{-1}) and 590 K (10 K s^{-1}) the Pd_2Si phase produces a coherent signal [Pd_2Si (00 16) reflection] that is clearly resolved in the XRD pattern.

The apparent delay between the calorimetric trace associated with silicide formation and the formation of Pd_2Si from the XRD spectra is mainly related to the minimum amount of material required to obtain a coherent signal from the Pd_2Si layer. In addition, as mentioned before, the strong variation of the thermal resistance during silicide formation alters the thermal profile measured by the nanocalorimeter. These variations make it difficult to use a suitable baseline to correct for heat losses and the addenda of the calorimetric cell, as clearly observed from the negative slope before the onset of the transformation at 420–425 K in the trace recorded at 0.1 K s^{-1} (Fig. 4*a*).

Fig. 5 shows individual X-ray spectra obtained during the thermal treatments with acquisition times of one frame every 10 K for the samples measured at 1 and 10 K s^{-1} and one frame every 2 K for the sample measured at 0.1 K s^{-1}. Before and after every experiment, more accurate XRD spectra with exposure times of about 100 s were acquired. From these spectra it is deduced that Pd_2Si was the only crystalline phase formed during silicide formation. Fig. 5(*a*) shows the as-deposited Pd/a-Si bilayer on the calorimetric chip as well as the product of the reaction after heating the sample to high temperature at 1 K s^{-1}. The Pd (111) reflection at 21.30° superposed on the Pt (111) diffraction peak at 21.15° is clearly resolved. After the thermal treatment, the Pd (111) peak

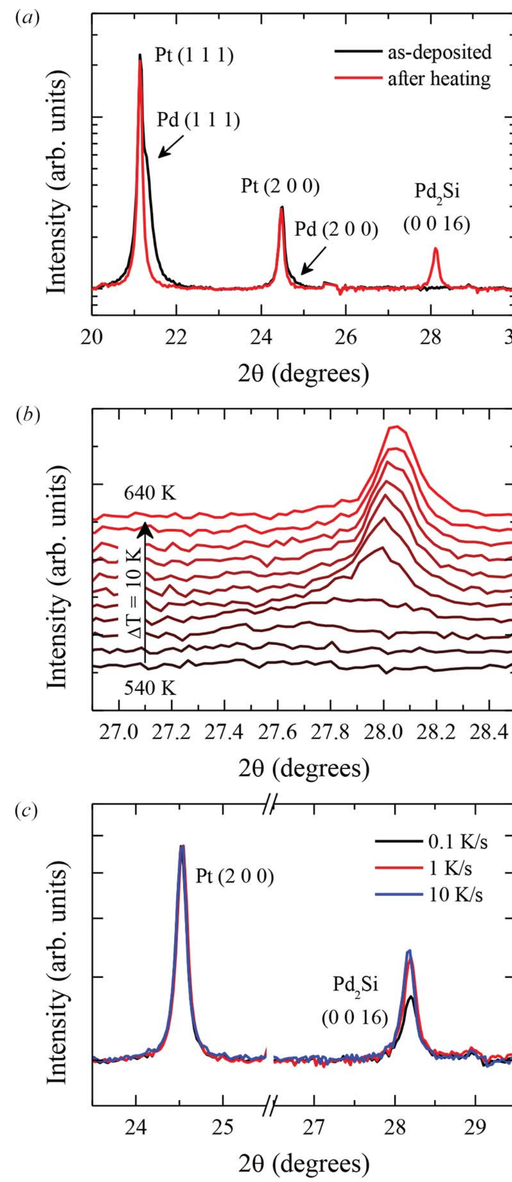

Figure 5
(*a*) X-ray diffraction patterns acquired for 100 s exposure corresponding to the same sample: prior to the heat treatment (black line) and after it (red line). (*b*) X-ray diffraction patterns acquired every 10 s for the sample measured at 1 K s^{-1}. The patterns obtained every 10 K from 540 to 640 K are stacked vertically to show the evolution of the Pd_2Si structure formation with temperature. (*c*) X-ray diffraction patterns acquired for 100 s exposure after the thermal treatment carried out at three different heating rates: 0.1 (black line), 1 (red line) and 10 K s^{-1} (blue line).

disappears and a new peak at 28.15° assigned to the Pd_2Si (0 0 16) reflection appears. The {00*l*} family of planes is the only one that appears in the entire diffractogram, which indicates a strong texture in the [00*l*] direction. Fig. 5(*b*) illustrates the evolution of the Pd_2Si (0 0 16) diffraction peak as a function of temperature during a temperature up-scan at 1 K s^{-1}. Every spectrum is recorded with a temperature shift of 10 K. During heating, the palladium diffraction signal remains unaltered up to 530 K and then it starts to disappear gradually up to 590 K, when it disappears completely. After the palladium signature begins to fade, the Pd_2Si structure

Table 1
Parameters obtained from nanocalorimetric and XRD patterns.

β is the heating rate, $T^{\rm cryst}$ is the temperature of crystallization, FWHM is the full width at half-maximum and θ_C is the centre of the Pd_2Si diffraction peak. The parameters FWHM and θ_C have been obtained by fitting a Lorentzian function to the experimental signal. Finally, $d^{\rm mean}$ is the mean size of the ordered domains calculated using the Scherrer equation.

β (K s^{-1})	$T^{\rm cryst}$ (K)	FWHM (°)	θ_C (°)	$d^{\rm mean}$ (nm)
0.1	506 ± 10	0.20 ± 0.02	14.08 ± 0.01	22.3 ± 0.4
1	535 ± 12	0.16 ± 0.02	14.08 ± 0.01	28.2 ± 0.6
10	559 ± 13	0.15 ± 0.02	14.07 ± 0.01	30.2 ± 0.7

starts to diffract from 560 K to 640 K, when it is completely formed (Fig. 5*b*). The displacement of the peaks due to the thermal expansion of the unit cell has been corrected. This fact shows that during silicide formation the Pd_2Si structure suffers a contraction as the temperature rises. The Pd_2Si unit cell undergoes a reduction along the *c* axis of 41.6 ± 5.4 pm between the {00*l*} planes during its formation, which is ~1.5% of the cell parameter length. Now, comparing the XRD patterns for the samples measured at three different heating rates, we observe a subtle difference on the resulting Pd_2Si reflection (Fig. 5*c*). By using the Scherrer equation (Scherrer, 1918) with the Pd_2Si (0 0 16) reflection, we estimate the mean coherent domains in a direction that is perpendicular to the substrate. As apparent from Fig. 5(*c*), the ordered domains increase with heating rate from 22 nm at 0.1 K s^{-1} to 30 nm at 10 K s^{-1} (Table 1). In all cases, the average size is smaller than the Pd_2Si layer thickness, ~100 nm, which confirms the samples are polycrystalline with a strong texture along the [00*l*] direction. These parameters have been obtained by fitting the peaks with a Lorentzian function. These results as well as the temperature of the calorimetric peak minimum are summarized in Table 1.

4. Conclusions

A combination of membrane-based nanocalorimetry and XRD techniques has been developed to characterize phase transformation during thin-film reactions. While nanocalorimetry provides information about the kinetics and thermodynamics of phase formation, XRD shows the structural characteristics of the phases. In this example, simultaneous nanocalorimetry and synchrotron X-ray diffraction have been used to characterize the formation of Pd_2Si through the reaction of thin films of Pd and a-Si. The combined use of both techniques allows the simultaneous determination of the structural variations of the sample together with the kinetics associated with phase formation. Calorimetry indicates that silicide formation is kinetically activated with different processes overlapping to produce a single broad calorimetric peak. The XRD data show how the structure is compressed along the basal plane, in the [00*l*] direction, when formed. No differences in the crystalline structure have been observed for samples heated at 0.1, 1 and 10 K s^{-1}, except for a small variation on the mean size of the ordered domains, which increases with the heating rate. The Pd_2Si thin films are polycrystalline and textured along the [00*l*] direction.

Acknowledgements

The authors acknowledge MAT2010-15202 and MAT2013-40896-P. PFV thanks MINECO for a FPU fellowship. We thank Theo Bijvoets from Rivac Technology for technical support and the fabrication of the vacuum chamber. These experiments were performed at the MSPD beamline at the ALBA synchrotron with the collaboration of the ALBA staff.

References

Gregoire, J. M., McCluskey, P. J., Dale, D., Ding, S., Schroers, J. & Vlassak, J. J. (2012). *Scr. Mater.* **66**, 178–181.
Knapp, M., Peral, I., Nikitina, L., Quispe, M. & Ferrer, S. (2011). *Z. Kristallogr. Proc.* **1**, 137–142.
Leon-Gutierrez, E., Garcia, G., Lopeandia, A. F., Clavaguera-Mora, M. T. & Rodríguez-Viejo, J. (2010). *J. Phys. Chem. Lett.* **1**, 341–345.
Lexa, D. (1999). *Rev. Sci. Instrum.* **70**, 2242.
Lopeandía, A. F., Cerdó, L. I., Clavaguera-Mora, M. T., Arana, L. R., Jensen, K. F., Muñoz, F. J. & Rodríguez-Viejo, J. (2005). *Rev. Sci. Instrum.* **76**, 065104.
Lopeandía, A. F., Pi, F. & Rodriguez-Viejo, J. (2008*a*). *Appl. Phys. Lett.* **92**, 122503.
Lopeandía, A. F., Valenzuela, J. & Rodríguez-Viejo, J. (2008*b*). *Sens. Actuators A*, **143**, 256–264.
Ma, E., Thompson, C. V. & Clevenger, L. A. (1991). *J. Appl. Phys.* **69**, 2211.
Marcelli, A., Innocenzi, P., Malfatti, L., Newton, M. A., Rau, J. V., Ritter, E., Schade, U. & Xu, W. (2012). *J. Synchrotron Rad.* **19**, 892–904.
Michaelsen, C., Barmak, K. & Weihs, T. P. (1997). *J. Phys. D*, **30**, 3167–3186.
Molina-Ruiz, M., Lopeandía, A. F., Gonzalez-Silveira, M., Garcia, G., Peral, I., Clavaguera-Mora, M. T. & Rodríguez-Viejo, J. (2014). *Appl. Phys. Lett.* **105**, 013113.
Molina-Ruiz, M., Lopeandía, A. F., Pi, F., Givord, D., Bourgeois, O. & Rodríguez-Viejo, J. (2011). *Phys. Rev. B*, **83**, 140407.
Nemouchi, F., Mangelinck, D., Bergman, C., Gas, P. & Smith, U. (2005). *Appl. Phys. Lett.* **86**, 041903.
Orava, J., Greer, A. L., Gholipour, B., Hewak, D. W. & Smith, C. E. (2012). *Nat. Mater.* **11**, 279–283.
Putero, M., Duployer, B., Blum, I., Ouled-Khachroum, T., Coulet, M.-V., Perrin, C., Ziegler, E., Muller, C. & Mangelinck, D. (2013). *Thin Solid Films*, **541**, 21–27.
Rosenthal, M., Doblas, D., Hernandez, J. J., Odarchenko, Y. I., Burghammer, M., Di Cola, E., Spitzer, D., Antipov, A. E., Aldoshin, L. S. & Ivanov, D. A. (2014). *J. Synchrotron Rad.* **21**, 223–228.
Scherrer, P. (1918). *Math. Klass.* **2**, 98–100.
Smeets, D., Demeulemeester, J., Deduytsche, D., Detavernier, C., Comrie, C. M., Theron, C. C., Lavoie, C. & Vantomme, A. (2008). *J. Appl. Phys.* **104**, 103538.
Spaepen, F. & Thompson, C. V. (1989). *Appl. Surf. Sci.* **38**, 1–12.
Xiao, K., Gregoire, J. M., McCluskey, P. J., Dale, D. & Vlassak, J. J. (2013). *J. Appl. Phys.* **113**, 243501.
Zalden, P., Aquilanti, G., Prestipino, C., Mathon, O., André, B., Wuttig, M. & Coulet, M.-V. (2012). *J. Synchrotron Rad.* **19**, 806–813.
Zhang, M., Efremov, M. Y., Olson, E., Zhang, Z. S. & Allen, L. H. (2002). *Appl. Phys. Lett.* **81**, 3801.